In the present arrangement, box 3 corresponds to the segment of the San Andreas fault with the greatest spatial clustering of microearthquakes, whereas boxes 2 and 4 contain less clustering (Fig. 1, A and B). In considering this difference, we have noted that the boundary between box 2 and box 3 lies in the area of significant geological changes along the San Andreas fault (*6*, *7*). These changes include (i) the appearance of Franciscan rocks in contact with the fault zone at the surface, which does not occur to the south; (ii) the northward merging of the Table Mountain fault and Parkfield syncline with the San Andreas fault; and (iii) the northern topographic termination of Middle Mountain, under which at least the last few moderate Parkfield earthquakes have taken place (*1*, *2*, *8*). To the north of this area, the San Andreas fault slips mostly by creep, whereas to the south the creep rate declines, and slip on the fault is accommodated mainly by moderate earthquakes. Thus, the clustering of microearthquakes in box 3 may be related to the geometric interaction of faults or fault segments that also juxtapose rocks of different mechanical properties north and south of this region.

We propose that the episode of increased fault slip at Parkfield resulted from a stress diffusion process that originated somewhere below the seismically active region northwest of Parkfield. This proposal stems from the observation that the changes in cumulative moment that began in 1990 first took place in the northwest and then in the southeast. A linear fit across the contours in Fig. 3B suggests that the propagation speed of this process along the San Andreas fault is 30 to 50 km/year. This disturbance may not have originated on the San Andreas fault itself because the initial increase in earthquake-related slip took place outside of this fault zone (Fig. 2).

The southeastward movement of earthquake activity at Parkfield is not without precedent. A series of $M \geq 4$ foreshocks that evidently moved southeastward toward the location of the main shocks were associated with both the 1934 and 1966 Parkfield $M > 5$ earthquakes (*1*, *8*, *9*). These foreshocks took place over the period of a couple of months and spanned 15 km of the fault, suggesting a stress disturbance that propagated at speeds of 60 to 100 km/year. Stress disturbances with propagation speeds even larger than these—approximately 100 to 200 km/year—have also been suggested for event sequences that have been observed in Turkey and China (*10*, *11*).

We have considered our observations in the light of a mechanical model for stress diffusion along a rupturing plate boundary like that of the San Andreas fault (*12*). In the stress diffusion model, the critical parameter is the propagation speed of the type of deformation front that drives the microearthquake activity. Theoretical analysis of stress relaxation below the seismogenic zone of a rupturing boundary indicates that when the stress diffusion speeds are reduced to less than 100 to 200 km/year by overlying fault asperities (strong inhomogeneities in fault strength), the result is elastic loading of these features (*12*). In our model, the rate of this loading would be proportional to the rate of the fault's microearthquake activity and the trend of the cumulative moment. Continued monitoring of the magnitude-latitude-time character of microearthquakes might thus detect a loading event that could cause the next moderate Parkfield earthquake.

REFERENCES AND NOTES

1. W. H. Bakun and T. V. McEvilly, *Science* **205**, 1375 (1979).
2. ———, *J. Geophys. Res.* **89**, 3051 (1984).
3. W. H. Bakun and A. G. Lindh, *Science* **229**, 619 (1985).
4. P. E. Malin, S. N. Blakeslee, M. G. Alvarez, A. J. Martin, *ibid.* **244**, 557 (1989).
5. The moments used in generating Fig. 2 represent average values that were observed at no fewer than three stations. The station moment for each event was calculated by integrating the S-wave displacement and velocity spectra over frequency and by assuming that the resulting values fit a frequency-squared model of the earthquake source. Summing these moments as a function of time yields the curves in Fig. 2. For reference to this method, see D. J. Andrews [in *Earthquake Source Mechanics*, K. Aki and P. Richards, Eds., *American Geophysical Union Monograph 37* (American Geophysical Union, Washington, DC, 1986)].
6. J. D. Sims, *U.S. Geol. Surv. Misc. Field Studies Map MF-2115* (1990).
7. W. R. Dickinson, *Geol. Soc. Am. Bull.* **77**, 707 (1966).
8. T. V. McEvilly, W. H. Bakun, K. B. Casaday, *Bull. Seismol. Soc. Am.* **57**, 1221 (1967).
9. A. G. Lindh and D. M. Boore, *ibid.* **71**, 95 (1981).
10. N. Toksoz *et al.*, *Pure Appl. Geophys.* **117**, 1258 (1979).
11. C. H. Scholz, *Nature* **267**, 121 (1977).
12. F. K. Lehner, V. C. Li, J. R. Rice, *J. Geophys. Res.* **86**, 6155 (1981).

13. We thank numerous colleagues at the University of California at Berkeley and at the U.S. Geological Survey, with whom we have shared the effort of keeping the Parkfield downhole seismology project alive. We also thank an anonymous reviewer, R. Simpson, and K. Malin for suggesting major improvements to the text. This work was supported by U.S. Geologic Survey grant 14-08-0001-G1375.

23 December 1991; accepted 12 March 1992

Electron-Tunneling Pathways in Cytochrome c

Deborah S. Wuttke, Morten J. Bjerrum,* Jay R. Winkler, Harry B. Gray†

Distant Fe^{2+}-Ru^{3+} electronic couplings have been extracted from intramolecular electron-transfer rates in Ru(histidine^{X}) (where X = 33, 39, 62, and 72) derivatives of cytochrome c. The couplings increase according to 62 (0.0060) < 72 (0.057) < 33 (0.097) < 39 (0.11 per wave numbers); however, this order is out of line with the histidine to heme edge-edge distances [62 (14.8) > 39 (12.3) > 33 (11.1) > 72 (8.4 angstroms)]. The rates (and the couplings) correlate with the lengths of σ-tunneling pathways comprised of covalent bonds, hydrogen bonds, and through-space jumps from the histidines to the heme group. Space jumps greatly decrease couplings: One from Pro^{71} to Met^{80} extends the σ-tunneling length of the His^{72} pathway by roughly 10 covalent-bond units.

Both theoretical (*1*–*11*) and experimental (*11*–*16*) studies have indicated that variations in distant electronic couplings could play a major role in controlling the rates of electron transfer (ET) through proteins. The most attractive theoretical formulations are ones that explicitly include the structure of the intervening polypeptide (*4*–*11*); of these, the Beratan, Betts, and Onuchic (BBO) coupling maps (*4*) have proved particularly useful in designing experimental systems for study. In the BBO map for cytochrome c, there are several regions on the protein surface where the calculated couplings to the heme are substantially different from those given by an exponential-decay-with-distance model (*4*). A main goal of our work on $Ru(bpy)_2(im)(His^X)^{2+}$ (bpy is 2,2′ bipyridine, im is imidazole) derivatives (*17*) of structurally engineered cytochromes c is to develop an experimentally validated coupling map for this protein. Here we report on four regions of the map (X = 33, 39, 62, and 72).

Histidines 33, 39, 62, and 72 [33 (horse heart) (*17*); 39 (*Candida krusei*) (*18*); 62 (genetically engineered $Asn^{62} \rightarrow$ His *Saccharomyces cerevisiae*) (*19*); and 72 (semisynthetic $Lys^{72} \rightarrow$ His horse heart) (*20*)] (Fig. 1) were modified by the $Ru(bpy)_2(CO_3)$-im procedure (*17*) to give $Ru(bpy)_2(im)(His^X)$-protein derivatives (*21*). Intramolecular ET

Beckman Institute, California Institute of Technology, Pasadena, CA 91125.

*Present address: Department of Chemistry, Royal Veterinary and Agricultural University, Thorvaldsensvej 40, 1871 Frederiksberg C, Denmark.
†To whom correspondence should be addressed.

Table 1. ET parameters for $Ru(bpy)_2(im)(His^X)$-cytochromes c. Numbers in parentheses indicate uncertainties in the preceding digits.

X	$*Ru(bpy)_2(im)(His^X)^{2+} \rightarrow Fe^{3+}$ k (s^{-1})	$Fe^{2+} \rightarrow Ru(bpy)_2(im)(His^X)^{3+}$ k (s^{-1})	k_{max} (s^{-1})	$(Fe^{2+}\text{-}Ru^{3+})$ H_{AB} (cm^{-1})	d (Å)	$\sigma\ell$ (Å)
39	$1.4(5) \times 10^6$	$3.2(4) \times 10^6$	3.3×10^6	0.11	12.3	19.6
33	$2.0(5) \times 10^5$	$2.6(3) \times 10^6$	2.7×10^6	0.097	11.1	19.5
72	$3.4(7) \times 10^5$	$9.0(3) \times 10^5$	9.4×10^5	0.057	8.4	24.6
62	$1.1(2) \times 10^5$	$1.0(2) \times 10^4$	1.0×10^4	0.0060	14.8	28.8

rates from Fe^{2+} to $Ru(bpy)_2(im)(His^X)^{3+}$ (Gibbs free energy $-\Delta G° = 0.74$ eV) (*17*) were measured by time-resolved absorption spectroscopy (*22*). Because the $Fe^{2+} \rightarrow Ru^{3+}$ ET reactions are nearly activationless (*23*), the maximum ET rates ($k_{max} = k$ at $-\Delta G°$ = the reorganization energy λ) are nearly the same as the experimentally measured rates (Table 1).

Semiclassical theory predicts that k_{max} values will fall off exponentially with distance (*1*). If we assume a maximum ET rate of 3×10^{12} s^{-1} at close contact (distance d = 3 Å), the edge-edge distance dependences for covalently coupled donor-acceptor complexes are represented adequately by lines with slopes of 0.8 to 1.2 $Å^{-1}$ (Fig. 2A) (*1*, *24*). Because the maximum ET rates for all the $Ru(bpy)_2(im)(His^X)$-modified cytochromes lie well below these lines, it is apparent that the Fe^{2+}-Ru^{3+} electronic couplings are weaker than the corresponding donor-acceptor interactions in purely covalently coupled systems. If we draw a best fit line through the $Fe^{2+} \rightarrow Ru^{3+}$ points (dots, Fig. 2A), its 3 Å intercept (1.6×10^8 s^{-1}) is much smaller than that expected for a system in which the terminal atoms of the bridging group are covalently bonded to the donor [Fe^{2+} (heme c)] and the acceptor [$Ru^{3+}(His^X)$]. Thus, none of the edge-edge exponential-decay models is satisfactory (*25*).

We find that the maximum ET rates correlate with a bond-length scale that takes into account the weaker couplings associated with hydrogen bonds and through-space jumps in dominant pathways (Fig. 1). The best pathway for His^{33} has 11 covalent bonds and a hydrogen bond (3.16 Å) that is equivalent to 2.9 covalent bonds. The dominant His^{62}-heme pathway includes 16 covalent bonds and 2 hydrogen bonds (*26*), and the His^{39}-heme pathway has 11 covalent bonds and a hydrogen bond. Of special interest is the finding that there are no good routes to couple His^{72} to the heme. The Met^{80} side of the heme has predominantly through-space contacts with the helix containing His^{72}, and the best pathway goes from His^{72} through Pro^{71} with a space jump to Met^{80}. Although there are only 8 covalent bonds in this path, the 3.88 Å space jump adds 10.6 bond units to the σ-tunneling length. Multiplying the effective number of bonds by 1.4 Å per bond gives σ-tunneling lengths ($\sigma\ell$) for the four pathways that correlate well with the maximum ET rates (one-bond limit set at 3×10^{12} s^{-1}; slope of 0.71 $Å^{-1}$) (Fig. 2B). The 0.71 $Å^{-1}$ decay accords closely with related distance dependences for covalently coupled donor-acceptor molecules (*27*).

Rates for the excited-state ET reactions also are given in Table 1. These reactions involve ET from the coordinated bpy radical anion at the protein surface to the ferriheme and are highly exoergic ($-\Delta G° > \lambda$) (*17*, *28*). The relatively high rates of these reactions are of interest, because the ability to rapidly inject electrons into internal protein redox centers with laser pulses could provide a novel method for studying highly reactive species that often are encountered (or proposed as intermediates) in the catalytic reactions of metalloenzymes.

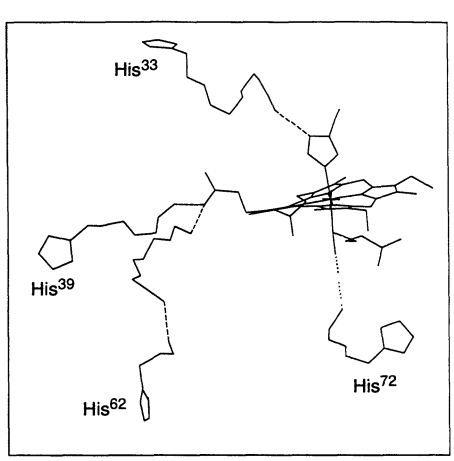

Fig. 1. Relative positions of the His^X groups and the heme unit in cytochrome c (*21*). Edge-edge distances (d) from the closest His^X ring atom to the Met^{80} sulfur or the closest His^{18} ring atom or porphyrin ring atom are as follows: $d(His^{72}\text{-}Met^{80})$ = 8.4; $d(His^{33}\text{-}His^{18})$ = 11.1; $d(His^{39}\text{-}porphyrin)$ = 12.3; $d(His^{62}\text{-}porphyrin)$ = 14.8 Å. Dominant σ-tunneling pathways from the imidazole to the heme based on BBO coupling calculations are shown (*4*): Covalent bonds are represented by solid lines, hydrogen bonds by dashed lines, and the space jump by a dotted line.

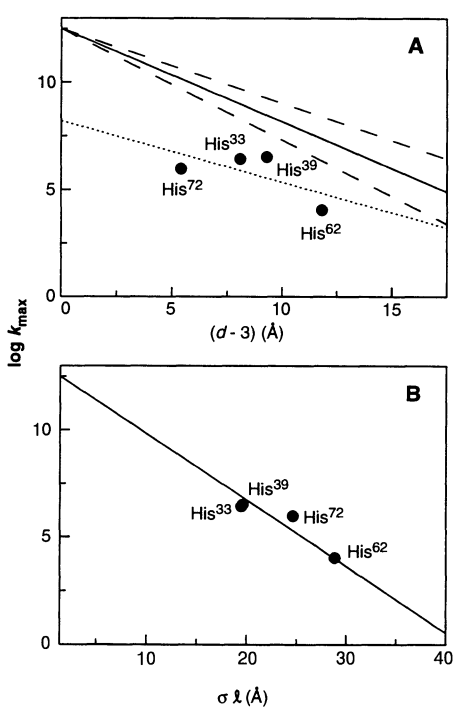

Fig. 2. (**A**) Maximum ET rates (X = 33, 39, 62, and 72) versus edge-edge distance (d) minus 3 Å (van der Waals contact). Exponential-decay lines: slope 1.0 $Å^{-1}$ (solid line); 0.8 to 1.2 $Å^{-1}$ (dashed lines); intercept 3×10^{12} s^{-1}. Best fit (dotted) line: slope 0.66 $Å^{-1}$; intercept 1.6×10^8 s^{-1}. (**B**) Maximum ET rates (X = 33, 39, 62, and 72) versus σ-tunneling length ($\sigma\ell$). slope 0.71 $Å^{-1}$; intercept 3×10^{12} s^{-1}.

REFERENCES AND NOTES

1. R. A Marcus and N Sutin, *Biochim. Biophys. Acta* **811**, 265 (1985)
2. P. Bertrand, in *Structure and Bonding*, G. A Palmer, Ed. (Springer-Verlag, Berlin, 1991), vol 75, pp. 1–47. A. Kuki, *ibid*, pp 49–83.
3. M A Ratner, *J Phys. Chem* **94**, 4877 (1990).
4. D N Beratan, J. N Betts, J N Onuchic, *Science* **252**, 1285 (1991)
5. D N Beratan, J N Onuchic, J N. Betts, B E. Bowler, H B Gray, *J Am Chem. Soc.* **112**, 7915 (1990). J N Onuchic, P C. P de Andrade, D. N Beratan, *J Chem Phys* **95**, 1131 (1991). J N Onuchic, D N Beratan, J R Winkler, H B Gray, *Annu Rev. Biophys Biomol Struct* **21**, 349 (1992). J N Betts, D N. Beratan, J N. Onuchic, *J Am. Chem Soc.*, in press. J. R. Winkler and H B. Gray, *Chem Rev*, in press
6. P Siddarth and R A Marcus, *J. Phys Chem* **94**, 8430 (1990)
7. A Broo and S. Larsson, *ibid.* **95**, 4925 (1991)
8. H E M Christensen, L. S. Conrad, K V Mikkelsen, M K Nielsen, J Ulstrup, *Inorg. Chem* **29**, 2808 (1990)
9. J M Gruschus and A. Kuki, in preparation
10. C Goldman, *Phys Rev A* **43**, 4500 (1991)
11. H Sigel and A Sigel, Eds., *Metal Ions in Biological Systems* (Dekker, New York, 1991), vol 27
12. M J Therien, J Chang, A. L Raphael, B E Bowler, H B Gray, in *Structure and Bonding*, G A Palmer, Ed (Springer-Verlag, Berlin, 1991), vol 75, pp 109–129. A. G. Sykes, *ibid*, pp 175–224
13. N. Liang, G Pielak, A G Mauk, M Smith, B. M Hoffman, *Proc Natl Acad. Sci U S A* **84**, 1249 (1987). N Liang *et al.*, *Science* **240**, 311 (1988). A M Everest *et al*, *J Am. Chem Soc* **113**, 4337 (1991)
14. G. McLendon. *Acc Chem Res* **21**, 160 (1988).
15. O Farver and I Pecht, *FEBS Lett* **244**, 376 (1989). *ibid*, p 379

16. B. A. Jacobs *et al.*, *J. Am. Chem. Soc.* **113**, 4390 (1991).
17. I.-J. Chang, J. R. Winkler, H. B. Gray, *ibid.*, p. 7056.
18. M. J. Therien, M. A. Selman, H. B. Gray, I.-J. Chang, J. R. Winkler, *ibid.* **112**, 2420 (1990).
19. B. E. Bowler, T. J. Meade, S. L. Mayo, J. H. Richards, H. B. Gray, *ibid.* **111**, 8757 (1989).
20. D. S. Wuttke, J. R. Winkler, H. B. Gray, in preparation.
21. The coordinates of the 1.94 Å structure of horse heart cytochrome c (His^{33} and His^{72} calculations) [G. W. Bushnell, G. V. Louie, G. D. Brayer, *J. Mol. Biol.* **214**, 585 (1990)] and the 1.23 Å structure of yeast-iso-1 cytochrome c (His^{39} and His^{62} calculations) [G. V. Louie and G. D. Brayer, *J. Mol. Biol.* **214**, 527 (1990)] were provided by G. D. Brayer. Energy minimization (*19*) of each structure with $Ru(bpy)_2(im)$ attached to His^X did not significantly change any edge-edge distance.
22. We measured rates of $Fe^{2+} \rightarrow Ru^{3+}$ ET using a flash-quench technique (*17*). We prepared metastable $Ru(bpy)_2(im)(His^X)^{3+}$-$Fe^{2+}$-cyt c in less than 100 ns by quenching a small fraction of $*Ru(bpy)_2(im)(His^X)^{2+}$-$Fe^{2+}$-cyt c with $Ru(NH_3)_6^{3+}$. Intramolecular $Fe^{2+} \rightarrow Ru^{3+}$ ET was readily observed at 550 and 400 nm (Fe^{2+}/Fe^{3+}) and 504 and 306 nm (Ru^{3+}/Ru^{2+}) after 480-nm excitation (~25-ns pulse width). Rates of intramolecular $*Ru^{2+} \rightarrow Fe^{3+}$ ET could not be determined directly from the $*Ru^{2+}$ decay kinetics because the rates are substantially slower than the intrinsic excited-state decay ($k_d = 1.4 \times 10^7\ s^{-1}$). Instead, $*Ru^{2+} \rightarrow Fe^{3+}$ ET rates were extracted from the yield of $Ru(bpy)_2(im)(His^X)^{3+}$-$Fe^{2+}$-cyt c [formed from $*Ru(bpy)_2(im)(His^X)^{2+}$-$Fe^{3+}$-cyt c].
23. According to semiclassical ET theory, rates become activationless when the reaction driving force ($-\Delta G^\circ$) equals the reorganization energy (λ) (*1*). This reorganization energy has been estimated to be 0.8 eV for $Ru(bpy)_2(im)(His)$-cyt c reactions (*17*). The activationless (maximum) rates are limited by an electronic factor,

$$k_{max} = (4\pi^3/h^2\ \lambda k_b T)^{1/2} H_{AB}^2$$

where k_b is Boltzmann's constant, T is temperature, h is Planck's constant, and H_{AB} is the matrix element that couples the reactants and products at the transition state.
24. B. E. Bowler, A. L. Raphael, H. B. Gray, *Prog. Inorg. Chem.* **38**, 259 (1990).
25. Activationless intraprotein ET spanning twelve orders of magnitude in rate and nearly 19 Å in redox-site separation has been interpreted in terms of edge-edge exponential decay with 1.4 $Å^{-1}$ slope and $1 \times 10^{13}\ s^{-1}$ intercept [C. C. Moser, J. M. Keske, K. Warncke, R. S. Farid, P. L. Dutton, *Nature* **355**, 796 (1992)]. Implicit in this interpretation is the assumption that the intervening polypeptide can be treated as a homogeneous medium. This correlation, then, serves as a reference line; deviations from this line indicate situations in which inhomogeneities of the intervening peptide must be considered. Because one (X = 72) of our k_{max} values falls four orders of magnitude below this edge-edge exponential-decay line, and two others (X = 33, 62) deviate from the line by more than a factor of 50, analysis in terms of the structure of the intervening medium is called for. In this context, it is of interest that calculations based on an inhomogeneous aperiodic lattice model give electronic couplings (X = 33, 39, 62) in good agreement with our experimentally derived values (*9*).
26. Another (nearly equivalent) pathway exists for His^{62} (*19*). The pathway consists of 12 covalent bonds and a space jump of 3.6 Å. The σ-tunneling length is 30.5 Å.
27. G. L. Closs and J. R. Miller, *Science* **240**, 440 (1988).
28. The electron donor in the $*Ru(bpy)_2(im)(His^X)^{2+}$ charge-transfer excited state is a bpy radical anion (*17*). The estimated order of H_{AB} values (62 ~ 33 ~ 72 < 39) for the bpy anion $\rightarrow Fe^{3+}$ ET reactions differs from that derived from the $Fe^{2+} \rightarrow Ru^{3+}$ rates. No interpretation of these couplings is offered; among the many uncertainties are the nature and magnitude of donor (bpy anion) couplings to groups on the protein surface.
29. We thank D. N. Beratan for assistance with the pathway analyses and for many helpful discussions. D.S.W. acknowledges an NSF predoctoral fellowship and a fellowship from the Parsons Foundation. M.J.B. was the Carlsberg Foundation Scholar in the Beckman Institute during 1990–91. Supported by National Science Foundation grants CHE-8822988 and CHE-9119992.

27 December 1991; accepted 10 March 1992

High-Resolution Imaging by Fourier Transform X-ray Holography

Ian McNulty,* Janos Kirz, Chris Jacobsen, Erik H. Anderson, Malcolm R. Howells,† Dieter P. Kern

Fourier transform x-ray holography has been used to image gold test objects with submicrometer structure, resolving features as small as 60 nanometers. The hologram-recording instrument uses coherent 3.4-nanometer radiation from the soft x-ray undulator beamline X1A at the National Synchrotron Light Source. The specimen to be imaged is placed near the first-order focal spot produced by a Fresnel zone plate; the other orders, chiefly the zeroth, illuminate the specimen. The wave scattered by the specimen interferes with the spherical reference wave from the focal spot, forming a hologram with fringes of low spatial frequency. The hologram is recorded in digital form by a charge-coupled device camera, and the specimen image is obtained by numerical reconstruction.

Soft x-ray microscopy offers the means to image thick, wet, unstained biological objects at high resolution with less damage than by electron probes (*1*, *2*). X-ray holographic microscopy offers good transverse and limited depth resolution from single exposures, is able to form both amplitude and phase-contrast images, and is amenable to flash exposure with pulsed sources. Fourier transform holography is especially suited to high-resolution x-ray imaging with digital recording and to rapid (minutes or less) numerical reconstruction of the holograms. We present experimental evidence that Fourier transform x-ray holography can operate near the resolution limit set by the optical design, which, in our case, is 60 nm.

Baez (*3*), Stroke (*4*), and Winthrop and Worthington (*5*) developed the conceptual foundations for x-ray holography and were among the first to advocate high-resolution holographic microscopy at x-ray wavelengths. Soon afterward, Rogers and Palmer (*6*) proposed the use of zone plates as beam splitters for x-ray holography. Following these and related theoretical developments, Aoki *et al.* (*7*) and Reuter and Mahr (*8*) performed pioneering demonstration experiments; they achieved modest resolution in spite of the severe limitations in coherent power then available. Subsequently, Kondratenko and Skrinsky (*9*) and Howells and Kirz (*10*) suggested that radiation from undulators in electron storage rings provides the required coherent flux for submicrometer holography and advocated the Fourier transform geometry with electronic detectors. Solem and co-workers (*11–13*) examined the possibilities of flash "snapshot" holography with x-ray lasers. They established requirements for coherence, power, and pulse length for successful imaging before the specimen is altered by motion, radiation damage, or thermal explosion. The flash approach potentially circumvents the damage issue and, in the case of the Fourier transform method, may result in lower average power levels on the detector. Haddad *et al.* (*14*) proposed flash x-ray holography with reflective reference scatterers, combined with charge-coupled device (CCD) detection.

Recently, undulator radiation has been used to demonstrate high-resolution Gabor x-ray holography (*15*) both at the National Synchrotron Light Source (NSLS) (*16*) and at Laboratoire d'Utilisation du Rayonnement Electromagnétique (LURE) (*17*). Biological specimens have been imaged with this technique at 56-nm resolution, and there are indications that the holograms contain information recorded near the ~20-nm resolution limit imposed by the photoresist detectors used (*16*). Using an x-ray laser to make 200-ps flash exposures, Trebes *et al.* (*18*) recorded Gabor holograms with 5-μm resolution. The attainable resolution with Gabor holography is ultimately limited to the detector resolution

I. McNulty, J. Kirz, C. Jacobsen, Physics Department, State University of New York, Stony Brook, NY 11794–3800.
E. H. Anderson and M. R. Howells, Lawrence Berkeley Laboratory, Berkeley, CA 94720.
D. P. Kern, IBM Thomas J. Watson Research Center, Yorktown Heights, NY 10598.

*To whom correspondence should be addressed at Advanced Photon Source, Argonne National Laboratory, 9700 South Cass Avenue, Argonne, IL 60439.
†Currently on leave at European Synchrotron Radiation Facility, BP220, 38043 Grenoble, France.